

On the Geometric Coherence of Global Aggregation in Federated Graph Neural Networks

Chethana Prasad Kabgere¹, Shylaja S S²

¹Department of Computer Science, Research Scholar, PES University, Karnataka, India

²Department of Computer Science, Professor, PES University, Karnataka, India

Article Info

Article history:

Received Feb 04, 2026

Revised month dd, yyyy

Accepted month dd, yyyy

Keywords:

Federated GNN

Cross-Domain Federated GNN

Geometric Coherence

Federated IoT Framework

ABSTRACT

Federated Learning (FL) enables distributed training across multiple clients without centralized data sharing, while Graph Neural Networks (GNNs) model relational data through message passing. In federated GNN settings, client graphs often exhibit heterogeneous structural and propagation characteristics. When standard aggregation mechanisms are applied to such heterogeneous updates, the global model may converge numerically while exhibiting degraded relational behavior. Our work identifies a geometric failure mode of global aggregation in Cross-Domain Federated GNNs. Although GNN parameters are numerically represented as vectors, they encode relational transformations that govern the direction, strength, and sensitivity of information flow across graph neighborhoods. Aggregating updates originating from incompatible propagation regimes can therefore introduce destructive interference in this transformation space. This leads to loss of coherence in global message passing. Importantly, this degradation is not necessarily reflected in conventional metrics such as loss or accuracy. To address this issue, we propose GGRS (Global Geometric Reference Structure), a server-side framework that regulates client updates prior to aggregation based on geometric admissibility criteria. GGRS preserves directional consistency of relational transformations as well as maintains diversity of admissible propagation subspaces. It also stabilizes sensitivity to neighborhood interactions, without accessing client data or graph topology. Experiments on six public benchmark graphs spanning citation, co-purchase, and co-authorship domains demonstrate that GGRS preserves global message-passing coherence across training rounds, highlighting the necessity of geometry-aware regulation in federated graph learning.

This is an open access article under the [CC BY-SA](#) license.



Corresponding Author:

Chethana Prasad Kabgere

Department of Computer Science, Research Scholar, PES University, Karnataka, India

Email: chethana1999@gmail.com

1. INTRODUCTION

Federated Learning (FL) addresses distributed optimization problems in which a shared model is trained across multiple decentralized clients under communication and data-access constraints [1]. At each communication round, locally optimized parameter updates are aggregated at a global server to form a new global model, which is subsequently broadcast to clients for further local optimization. Cross-domain federated machine learning [4] refers to a federated setting in which participating clients hold data originating from distinct domains or distributions, rather than being non-IID partitions of a single dataset. In this regime, each client's local data distribution may differ substantially in feature statistics, label semantics, or structural char-

Journal homepage:

acteristics, leading to stronger heterogeneity than conventional FL. The goal remains to learn a shared global model via decentralized optimization, but aggregation becomes more challenging due to domain-induced misalignment across client updates. Classical aggregation schemes such as Federated Averaging (FedAvg) implicitly assume that client updates lie in a common parameter space where linear combination preserves model semantics. GNNs [5] fundamentally violate this assumption. A GNN does not merely define a parameterized predictor, but rather a *parameterized message-passing operator* acting on graph-structured domains [5, 6]. For a fixed architecture, learnable parameters induce a family of linear and nonlinear operators that govern how node representations are updated as a function of neighborhood structure, aggregation depth, and interaction strength. Consequently, parameter updates in GNNs correspond to perturbations of an operator that determines the geometry of information flow over the graph, rather than independent numerical adjustments.

In federated GNN[2] settings, each client optimizes this operator with respect to its own graph distribution. Let $\mathcal{G}_k \sim \mathcal{D}_k$ denote the graph distribution observed by client k . Differences in topology, degree distribution, sparsity, and homophily across $\{\mathcal{D}_k\}$ induce *structurally distinct optimal message-passing operators*, even under a shared task objective [7]. Local training therefore shapes parameters toward client-specific propagation regimes, such as strong local aggregation, smooth long-range diffusion, or sparse selective propagation. These regimes correspond to distinct regions in the space of admissible operators. Standard global aggregation ignores this structure. We observe that by linearly averaging parameter updates, the server constructs a global parameter vector that is not guaranteed to correspond to a coherent message-passing operator for any of the underlying graph distributions. From an operator-theoretic perspective, this procedure amounts to mixing perturbations of distinct operators without enforcing compatibility of their dominant directions, invariant subspaces, or sensitivity profiles. Hence, the resulting global model may therefore exhibit *operator degeneration*, in which the induced message-passing transformation loses expressive capacity despite numerical convergence of parameters. This degeneration directly affects predictions. Inference in GNNs relies on the repeated application of the learned message-passing operator to propagate information across graph neighborhoods. We see that when aggregation disrupts the operator’s geometric structure, the global model can exhibit diminished sensitivity to graph perturbations, a collapse of effective propagation depth, or excessive contraction of node representations. These effects are closely related to over-smoothing and over-squashing phenomena studied in non-federated GNNs [8, 9]. Importantly, such failures may not immediately manifest in task loss or accuracy, as the model can still fit marginal label distributions while relying increasingly on non-relational cues. The impact of geometric degradation is amplified by the iterative nature of FL.

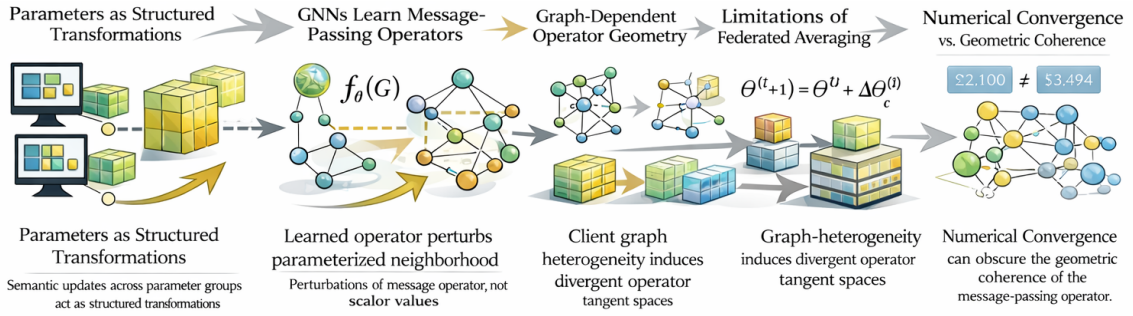
The global model produced by the server defines the initialization for all clients in the subsequent round. If this model encodes a distorted message-passing operator, local optimization must first compensate for this distortion before adapting to the local graph structure. This induces corrective gradients that are misaligned across clients, increasing update variance and amplifying destructive interference at the next aggregation step. Over multiple rounds, this feedback loop leads to progressive destabilization of the global operator, even as standard convergence criteria are satisfied. Existing approaches to federated GNN learning primarily address heterogeneity through personalization, client clustering, or adaptive weighting strategies [2, 13, 14]. While effective in mitigating performance degradation, these methods do not explicitly characterize aggregation as an operation on message-passing operators, nor do they impose constraints that preserve the geometric integrity of the induced transformations. As a result, failure modes arising from *operator-level incompatibility* rather than optimization error remain unaddressed.

Our work adopts a geometric perspective on federated GNN aggregation, viewing client updates as perturbations in the space of message-passing operators. From this viewpoint, effective aggregation requires preserving structural properties such as directional alignment of operator updates, consistency of dominant subspaces, and stability of sensitivity to neighborhood structure. This formulation motivates the development of server-side mechanisms that regulate aggregation to maintain operator coherence across heterogeneous clients, thereby preventing silent degradation of global message-passing capacity in federated GNNs.

1.1. Geometric Observations in Federated GNN

From our study, we have summarized a set of fundamental observations regarding the geometric behavior of GNN under federated aggregation. These observations are not specific to a particular architecture or optimization strategy, but arise from the interaction between graph-dependent message passing and parameter aggregation across heterogeneous clients.

Parameters as Structured Transformations: Although model parameters are numerically represented as vectors



Federated aggregation can degrade the graph-structured geometry of θ the learned message-passing operator.

Figure 1. Geometric observations in federated GNN.

or matrices, learning behavior does not arise from individual scalar values but from coordinated changes across parameter groups. In GNNs, parameters jointly define structured transformations that govern how information propagates across graph neighborhoods. Consequently, the semantic meaning of a parameter update is determined by its direction and interaction with other parameters, rather than by its magnitude alone.

GNNs Learn Message-Passing Operators: A GNN induces a parameterized message-passing operator whose repeated application updates node representations as a function of graph connectivity. In a fixed architecture, parameters specify how neighborhood information is aggregated, how far information propagates, and how sensitive node embeddings are to structural perturbations. Parameter updates therefore correspond to perturbations of this operator rather than independent numerical adjustments.

Graph-Dependent Operator Geometry: The operator induced by a GNN is graph-dependent. The same parameter configuration can induce distinct transformations when applied to graphs with different adjacency structures or feature distributions. As a result, the Jacobian of the GNN with respect to its parameters depends on the underlying graph, implying that parameter updates computed on different clients generally inhabit distinct operator tangent spaces.

Implicit Assumptions of Federated Averaging. Standard federated aggregation mechanisms implicitly assume that client updates are commensurate in a shared Euclidean parameter space, such that linear combination preserves model semantics. This assumption is violated in federated GNNs, where client updates encode perturbations of graph-dependent operators. Linear aggregation therefore mixes updates without enforcing compatibility of their induced transformations.

Numerical Convergence Versus Geometric Coherence. Federated training can exhibit numerical convergence in terms of loss reduction or gradient norms while simultaneously degrading the geometric coherence of the message-passing operator. Such degradation may manifest as diminished sensitivity to neighborhood structure, collapse of effective propagation depth, or contraction of representations into low-dimensional subspaces.

1.2. Limitations of Accuracy-Centric Evaluation in Federated GNNs

Machine learning systems are commonly evaluated using task-level metrics such as accuracy, F1-score, or loss. These metrics implicitly assume that improvements or degradation in model performance directly reflect the quality of the learned representations. While this assumption holds reasonably well for centralized learning on i.i.d. data, it becomes insufficient in federated and graph-based learning settings, where model behavior depends critically on relational structure and iterative aggregation dynamics.

Accuracy as a Performance Proxy in Conventional Learning. In conventional supervised learning, accuracy measures the alignment between model predictions and ground-truth labels on a fixed data distribution. Optimization procedures are designed to minimize empirical risk, and convergence in loss is typically interpreted as convergence in representation quality. Under these assumptions, parameter averaging or gradient-based updates preserve semantic meaning, and degradation in performance is readily observable through scalar metrics.

Limitations of Accuracy Metrics in GNNs. GNNs differ fundamentally from standard models in that predictions are produced through iterative message passing over graph structure. The expressive power of a GNN depends not only on parameter values, but on how those parameters govern information propagation across neighborhoods, graph depth, and connectivity patterns. As a result, a GNN can exhibit stable accuracy while its internal message-passing dynamics degrade. In particular, accuracy does not capture whether:neighborhood

information is meaningfully integrated or collapsed, long-range dependencies are preserved or suppressed, node representations remain sensitive to structural perturbations, propagation depth remains effective across layers. These properties are geometric and operator-level in nature, and their degradation may remain invisible to scalar evaluation metrics.

Accuracy Degradation in Federated Settings. In FL, accuracy is further confounded by the absence of a centralized validation distribution. Each client evaluates performance on its local data, and the global model is rarely assessed on a distribution that reflects the union of client graph structures. As a result, a global model may appear to perform adequately on average while being misaligned with all individual client distributions. Moreover, federated training introduces an iterative feedback loop: the global model is repeatedly broadcast to clients and used as the initialization for local optimization. Even small distortions in model behavior introduced by aggregation can compound over rounds, leading to progressive degradation that is not immediately reflected in early-round accuracy measurements. Empirically, federated GNNs under heterogeneous graph distributions exhibit several failure modes that are poorly explained by accuracy alone: Over-smoothing acceleration: node representations collapse into low-rank subspaces more rapidly than in centralized training. Over-squashing amplification: long-range information is increasingly compressed, reducing the effective receptive field. Update oscillation: local updates increasingly counteract global updates across rounds. Representation drift: the semantic meaning of intermediate embeddings changes across rounds despite stable task loss. These effects indicate degradation of the learned message-passing operator rather than simple underfitting or overfitting.

Root Cause: Aggregation-Induced Geometric Distortion. The common factor underlying these failure modes is the interaction of heterogeneous client updates at the global server. Client updates encode graph-dependent operator perturbations. Standard aggregation mechanisms combine these updates in parameter space without enforcing compatibility of their induced transformations. This process can converge numerically while simultaneously distorting the geometry of the global message-passing operator. Such distortion alters propagation directionality, collapses admissible subspaces, and destabilizes sensitivity to graph structure—effects that directly impair relational learning but may not immediately impact prediction accuracy. These observations indicate that federated GNN training cannot be reliably assessed or stabilized using accuracy-centric metrics alone. Scalar performance measures fail to diagnose degradation of message-passing geometry and provide no insight into the stability of relational representations across communication rounds. Consequently, effective federated GNN systems require mechanisms that explicitly preserve operator-level geometric coherence during aggregation. Without such mechanisms, improvements in optimization or personalization may address symptoms while leaving the underlying structural failure unresolved.

2. PROBLEM FORMULATION AND GEOMETRIC FAILURE IN FEDERATED GNN AGGREGATION

2.1. Federated GNN Learning Setup

We consider a federated learning (FL) system comprising K clients and a central server. Each client $k \in [K] \triangleq \{1, \dots, K\}$ holds a private graph

$$\mathcal{G}_k = (\mathcal{V}_k, \mathcal{E}_k, \mathbf{X}_k \in \mathbb{R}^{n_k \times d}, \mathbf{Y}_k), \quad (1)$$

drawn from a client-specific distribution \mathcal{D}_k . Heterogeneity is encoded by the assumption $\mathcal{D}_k \neq \mathcal{D}_{k'}$ for $k \neq k'$, arising from structural differences in graph topology, feature statistics, and label distributions.

All clients share a GNN architecture with parameter vector $\theta \in \mathbb{R}^p$. At communication round t , local training at client k solves

$$\theta_k^{(t)} = \arg \min_{\theta} \mathbb{E}_{\mathcal{G}_k \sim \mathcal{D}_k} [\mathcal{L}(f_{\theta}(\mathcal{G}_k), \mathbf{Y}_k)]. \quad (2)$$

Clients transmit parameter updates $\Delta\theta_k^{(t)} = \theta_k^{(t)} - \theta^{(t)}$ to the server, which forms the next global model via weighted aggregation:

$$\theta^{(t+1)} = \theta^{(t)} + \sum_{k=1}^K w_k \Delta\theta_k^{(t)}, \quad w_k \geq 0, \quad \sum_k w_k = 1. \quad (3)$$

2.2. GNN Parameters as Graph-Dependent Operator Families

An L -layer GNN is realized by iterated message-passing:

$$\mathbf{H}^{(l+1)} = \Phi_{\theta^{(l)}}(\mathbf{H}^{(l)}, \mathcal{G}), \quad l = 0, \dots, L-1, \quad \mathbf{H}^{(0)} = \mathbf{X}. \quad (4)$$

For a graph convolutional layer, $\Phi_{\theta}(\mathbf{H}, \mathcal{G}) = \sigma(\tilde{\mathbf{A}}\mathbf{H}\mathbf{W}_{\theta})$, where $\tilde{\mathbf{A}} = \hat{\mathbf{D}}^{-1/2}\hat{\mathbf{A}}\hat{\mathbf{D}}^{-1/2}$ is the symmetrically-normalized adjacency with self-loops. Let $\mathcal{T}_{\theta}^{\mathcal{G}} : \mathbb{R}^{n \times d} \rightarrow \mathbb{R}^{n \times c}$ denote the full L -layer operator induced by (θ, \mathcal{G}) .

A key structural observation is that θ does *not* specify a single fixed operator but rather an entire *family* $\{\mathcal{T}_{\theta}^{\mathcal{G}}\}_{\mathcal{G}}$, one member per graph. For distinct client graphs $\mathcal{G}_a \neq \mathcal{G}_b$,

$$\mathcal{T}_{\theta}^{\mathcal{G}_a} \neq \mathcal{T}_{\theta}^{\mathcal{G}_b}, \quad (5)$$

even though θ is identical. Consequently, the parameter space \mathbb{R}^P is not a neutral vector space: directions in \mathbb{R}^P carry different operational meaning depending on which graph they act upon.

2.3. Operator Perturbations and Geometric Incompatibility

For client k , a first-order expansion around $\theta^{(t)}$ gives

$$\mathcal{T}_{\theta^{(t)} + \Delta\theta_k}^{\mathcal{G}_k} \approx \mathcal{T}_{\theta^{(t)}}^{\mathcal{G}_k} + \underbrace{\mathcal{J}_{\theta^{(t)}}^{\mathcal{G}_k} \Delta\theta_k}_{\Delta\mathcal{T}_k}, \quad (6)$$

where $\mathcal{J}_{\theta}^{\mathcal{G}_k} \in \mathbb{R}^{(n_k c) \times P}$ is the Jacobian of the vectorized output with respect to θ on graph \mathcal{G}_k . The term $\Delta\mathcal{T}_k \triangleq \mathcal{J}_{\theta^{(t)}}^{\mathcal{G}_k} \Delta\theta_k$ is the *induced operator perturbation*: it lives in the tangent space of the operator manifold at $\mathcal{T}_{\theta^{(t)}}^{\mathcal{G}_k}$.

Equation (3) aggregates parameter vectors, yielding a global operator perturbation on any evaluation graph \mathcal{G} :

$$\Delta\mathcal{T}^{\mathcal{G}} = \mathcal{J}_{\theta^{(t)}}^{\mathcal{G}} \sum_{k=1}^K w_k \Delta\theta_k. \quad (7)$$

Because each $\Delta\theta_k$ was optimized under $\mathcal{J}_{\theta^{(t)}}^{\mathcal{G}_k}$ rather than $\mathcal{J}_{\theta^{(t)}}^{\mathcal{G}}$, the sum in (7) conflates vectors from geometrically incompatible tangent spaces. Unless $\mathcal{J}_{\theta^{(t)}}^{\mathcal{G}_k} \approx \mathcal{J}_{\theta^{(t)}}^{\mathcal{G}_{k'}}$ for all k, k' —an assumption that fails whenever clients differ substantially in graph structure [5, 7]—the resulting global operator lacks coherent directional structure.

Destructive interference. Consider two clients i, j satisfying

$$\langle \mathcal{J}_{\theta^{(t)}}^{\mathcal{G}_i} \Delta\theta_i, \mathcal{J}_{\theta^{(t)}}^{\mathcal{G}_j} \Delta\theta_j \rangle < 0. \quad (8)$$

Their combined contribution to $\Delta\mathcal{T}^{\mathcal{G}}$ partially cancels in operator space, even when $\|\Delta\theta_i\|$ and $\|\Delta\theta_j\|$ are each large. This cancellation reduces the effective rank and sensitivity of $\Delta\mathcal{T}^{\mathcal{G}}$, contracting message-passing dynamics in a manner invisible to parameter norms or training loss.

Training feedback amplification. The distorted $\theta^{(t+1)}$ is broadcast to all clients as the initialization for round $t+1$. Each client must now apply a corrective update to recover operator geometry suited to \mathcal{G}_k , but these corrective updates are themselves mutually misaligned, amplifying interference at the subsequent aggregation step. This feedback loop constitutes the central failure mode in heterogeneous federated GNN training.

This leads us to our problem statement: given a federated system with heterogeneous graph distributions $\{\mathcal{D}_k\}_{k=1}^K$, we are to design a server-side aggregation mechanism that preserves the geometric coherence of the induced message-passing operator—specifically, directional alignment, low-dimensional subspace structure, and sensitivity stability—across communication rounds, without access to client graphs or data.

3. FORMAL DERIVATION OF GEOMETRIC REGULATION IN FEDERATED GNN AGGREGATION

3.1. Federated Aggregation as Tangent-Space Averaging

Recall from (6) that local update $\Delta\theta_k$ induces an operator perturbation $\Delta\mathcal{T}_k = \mathcal{J}_\theta^{\mathcal{G}_k} \Delta\theta_k$. The FedAvg global perturbation is

$$\Delta\mathcal{T}^{\text{FedAvg}} = \sum_{k=1}^K w_k \mathcal{J}_\theta^{\mathcal{G}_k} \Delta\theta_k. \quad (9)$$

Equation (9) is a weighted sum of vectors from distinct tangent spaces $\{\mathcal{T}_\theta^{\mathcal{G}_k}\}$. Its deficiency can be quantified via the cosine misalignment:

$$\cos\angle(\Delta\mathcal{T}_i, \Delta\mathcal{T}_j) = \frac{\langle \mathcal{J}_\theta^{\mathcal{G}_i} \Delta\theta_i, \mathcal{J}_\theta^{\mathcal{G}_j} \Delta\theta_j \rangle}{\|\mathcal{J}_\theta^{\mathcal{G}_i} \Delta\theta_i\| \|\mathcal{J}_\theta^{\mathcal{G}_j} \Delta\theta_j\|}. \quad (10)$$

When (10) is negative for a significant fraction of client pairs, the aggregated perturbation suffers destructive interference as formalized in (8).

3.2. The Data-Free Proxy Map Ψ

The fundamental obstacle is that the server has no access to $\{\mathcal{G}_k\}$ and therefore cannot compute $\Delta\mathcal{T}_k$ exactly. We derive a data-free proxy $\widehat{\Delta\mathcal{T}}_k$ that captures the directional signature of $\Delta\mathcal{T}_k$ from $\Delta\theta_k$ alone.

Step 1: Factoring the Jacobian. Write the composite Jacobian as

$$\mathcal{J}_\theta^{\mathcal{G}_k} = \mathbf{P}_k \mathbf{Q}, \quad (11)$$

where $\mathbf{Q} \in \mathbb{R}^{p \times p}$ is a graph-independent component capturing global parameter sensitivity (e.g., $\mathbf{Q} = \mathbf{I}_p$ as the first-order approximation, or the empirical Fisher information matrix averaged across clients), and \mathbf{P}_k encodes the graph-specific modulation of propagation. Under moderate heterogeneity the dominant left singular subspace of \mathbf{P}_k is approximately shared across clients [7, 15], motivating the approximation

$$\mathcal{J}_\theta^{\mathcal{G}_k} \approx \mathbf{Q}, \quad \forall k \in [K]. \quad (12)$$

Step 2: Deriving the proxy direction. Under approximation (12), the induced operator perturbation reduces to

$$\Delta\mathcal{T}_k \approx \mathbf{Q} \Delta\theta_k. \quad (13)$$

Taking $\mathbf{Q} = \mathbf{I}_p$ as the canonical reference metric (corresponding to the limit of uniform parameter sensitivity), the directional component of the operator perturbation is characterized entirely by the unit vector

$$\mathbf{z}_k = \frac{\Delta\theta_k}{\|\Delta\theta_k\|_2} \in \mathbb{S}^{p-1}, \quad (14)$$

which belongs to the unit hypersphere in parameter space.

Step 3: Formal definition of Ψ . We define the *data-free proxy map*

$$\Psi : \Delta\theta_k \mapsto \widehat{\Delta\mathcal{T}}_k \triangleq \frac{\Delta\theta_k}{\|\Delta\theta_k\|_2}, \quad (15)$$

mapping each transmitted update to its unit-normalized direction in parameter space. Ψ is well-defined for $\Delta\theta_k \neq \mathbf{0}$ and requires only the transmitted update vector; it does not access \mathcal{G}_k .

Remark 1. *The identity approximation $\mathbf{Q} = \mathbf{I}_p$ is used throughout for tractability. When a global estimate of the Fisher information matrix $\hat{\mathbf{F}}$ is available (e.g., from a proxy dataset), one may use $\Psi(\Delta\theta_k) = \hat{\mathbf{F}}^{1/2} \Delta\theta_k / \|\hat{\mathbf{F}}^{1/2} \Delta\theta_k\|_2$, which weights parameter directions by their sensitivity and provides a tighter proxy. The identity case is equivalent to treating all parameter dimensions as equally informative, which is a standard assumption in parameter-space federated averaging.*

3.3. Reference Direction and Geometric Admissibility

Constructing the reference operator direction. Given the proxy vectors $\{\mathbf{z}_k^{(t)}\} = \{\Psi(\Delta\theta_k^{(t)})\}$, we maintain an exponential moving average (EMA) reference direction tracking the dominant aggregated perturbation over time:

$$\mathbf{r}^{(t)} = \alpha \mathbf{r}^{(t-1)} + (1 - \alpha) \sum_{k=1}^K w_k \mathbf{z}_k^{(t)}, \quad \mathbf{r}^{(0)} = \mathbf{0}, \quad (16)$$

with decay parameter $\alpha \in (0, 1)$. After normalization, the unit reference vector is

$$\hat{\mathbf{r}}^{(t)} = \frac{\mathbf{r}^{(t)}}{\|\mathbf{r}^{(t)}\|_2 + \epsilon_0}, \quad \epsilon_0 > 0 \text{ (numerical stabilizer)}. \quad (17)$$

The EMA in (16) serves as a server-side estimate of the *admissible* operator perturbation direction: it accumulates the weighted consensus of past proxy directions, giving more weight to recent rounds via α .

Three geometric admissibility constraints. We characterize coherence of an operator perturbation $\widehat{\Delta\mathcal{T}}_k$ relative to $\hat{\mathbf{r}}^{(t)}$ through three structural conditions.

C1 (Directional Consistency). The cosine alignment of client k 's proxy with the reference direction is

$$\gamma_k^{(t)} = \langle \mathbf{z}_k^{(t)}, \hat{\mathbf{r}}^{(t)} \rangle = \cos \angle(\Delta\theta_k^{(t)}, \mathbf{r}^{(t)}). \quad (18)$$

A client is deemed *directionally consistent* if $\gamma_k^{(t)} \geq 0$. When $\gamma_k^{(t)} < 0$, the induced operator perturbation is *antidirectional* to the global consensus—its inclusion in aggregation constitutes destructive interference as in (8).

C2 (Subspace Compatibility). Let $\mathcal{B}^{(t)} = \{\mathbf{z}_k^{(s)} : s \in \mathcal{W}^{(t)}, k \in [K]\}$ denote the sliding buffer of proxy directions over a recent window $\mathcal{W}^{(t)}$, and form the matrix $\mathbf{Z}^{(t)} \in \mathbb{R}^{p \times |\mathcal{B}^{(t)}|}$. The *admissible subspace* is defined as the column space of the leading q right singular vectors:

$$\mathbf{Z}^{(t)} = \mathbf{U}^{(t)} \boldsymbol{\Sigma}^{(t)} \mathbf{V}^{(t)\top}, \quad \mathcal{S}^{(t)} = \text{col}(\mathbf{U}_{:,1:q}^{(t)}) \subset \mathbb{R}^p, \quad (19)$$

capturing the q dominant modes of variation in historical proxy directions. The orthogonal projector onto $\mathcal{S}^{(t)}$ is

$$\mathbf{\Pi}_{\mathcal{S}^{(t)}} = \mathbf{U}_{:,1:q}^{(t)} \mathbf{U}_{:,1:q}^{(t)\top}. \quad (20)$$

A proxy direction satisfies subspace compatibility if $\mathbf{\Pi}_{\mathcal{S}^{(t)}} \mathbf{z}_k^{(t)}$ retains significant energy, i.e., components outside $\mathcal{S}^{(t)}$ are treated as noise arising from client-specific graph artifacts rather than globally informative signal.

C3 (Sensitivity Stability). We impose an ℓ_2 -norm bound on the regulated proxy:

$$\|\widehat{\Delta\mathcal{T}}_k^{\text{reg}}\|_2 \leq \varepsilon, \quad (21)$$

preventing any single client from dominating the aggregated operator perturbation through an abnormally large update magnitude. This bound also limits the sensitivity of the global operator to adversarial or outlier clients.

3.4. Derivation of the Geometric Regulation Operator \mathcal{R}

Given the three admissibility conditions C1–C3, we now derive $\mathcal{R} : \mathbb{R}^p \rightarrow \mathbb{R}^p$ as the composition of three sequentially applied operations.

Step 1: Directional attenuation (enforcing C1). Define the attenuation factor

$$\beta_k^{(t)} = \begin{cases} 1, & \text{if } \gamma_k^{(t)} \geq 0 \text{ or } t \leq w, \\ \beta(1 - \gamma_k^{(t)}), & \text{if } \gamma_k^{(t)} < 0 \text{ and } t > w, \end{cases} \quad (22)$$

where $\beta \in (0, 1)$ is the attenuation strength hyperparameter and w is a warm-up period allowing $\hat{\mathbf{r}}^{(t)}$ to stabilize. Note that $\gamma_k^{(t)} < 0$ implies $1 - \gamma_k^{(t)} > 1$, so $\beta_k^{(t)} \in (0, 2\beta)$; in practice we additionally clamp $\beta_k^{(t)} \leq \beta_{\max} < 1$ to avoid full suppression. The attenuated proxy is

$$\tilde{\mathbf{z}}_k^{(t)} = \beta_k^{(t)} \mathbf{z}_k^{(t)}. \quad (23)$$

By construction, $\langle \tilde{\mathbf{z}}_k^{(t)}, \hat{\mathbf{r}}^{(t)} \rangle = \beta_k^{(t)} \gamma_k^{(t)}$. When $\gamma_k^{(t)} < 0$, the attenuation strictly reduces the magnitude of the antidirectional contribution without forcing it to zero, preserving a fraction of the client's update to avoid complete exclusion.

Step 2: Subspace projection (enforcing C2). Project the attenuated proxy onto the admissible subspace:

$$\hat{\mathbf{z}}_k^{(t)} = \mathbf{\Pi}_{\mathcal{S}^{(t)}} \tilde{\mathbf{z}}_k^{(t)} = \mathbf{U}_{:,1:q}^{(t)} \mathbf{U}_{:,1:q}^{(t)\top} \tilde{\mathbf{z}}_k^{(t)}. \quad (24)$$

This discards components of $\Delta\theta_k$ that lie outside the dominant q -dimensional subspace of recent consensus directions, removing client-idiosyncratic noise orthogonal to the historical aggregation manifold.

Step 3: Sensitivity clipping (enforcing C3). The regulated proxy is obtained by rescaling the projected direction to satisfy the sensitivity bound:

$$\widehat{\Delta\mathcal{T}}_k^{\text{reg}} = \min\left(1, \frac{\varepsilon}{\|\hat{\mathbf{z}}_k^{(t)}\|_2 + \epsilon_0}\right) \hat{\mathbf{z}}_k^{(t)}. \quad (25)$$

Clipping is norm-preserving in direction and acts only when $\|\hat{\mathbf{z}}_k^{(t)}\|_2 > \varepsilon$.

Composition: the regulation operator. Combining Steps 1–3, the geometric regulation operator \mathcal{R} is defined as the composition

$$\mathcal{R}(\Delta\theta_k^{(t)}) \triangleq \min\left(1, \frac{\varepsilon}{\|\hat{\mathbf{z}}_k^{(t)}\|_2 + \epsilon_0}\right) \mathbf{\Pi}_{\mathcal{S}^{(t)}} \left[\beta_k^{(t)} \Psi(\Delta\theta_k^{(t)}) \right], \quad (26)$$

which operates solely on the transmitted $\Delta\theta_k^{(t)}$ and the server-maintained quantities $\hat{\mathbf{r}}^{(t)}$ and $\mathbf{\Pi}_{\mathcal{S}^{(t)}}$. The regulated global update is

$$\Delta\theta^{\text{global}} = \sum_{k=1}^K w_k \mathcal{R}(\Delta\theta_k^{(t)}). \quad (27)$$

3.5. Theoretical Properties of \mathcal{R}

We now show that the global operator perturbation produced by (27) satisfies all three admissibility conditions by construction.

Proposition 1 (Geometric Admissibility of Regulated Aggregation). *Let $\Delta\theta^{\text{global}}$ be given by (27) with \mathcal{R} as in (26). Define the regulated global proxy $\Delta\mathcal{T}^{\text{reg}} = \sum_{k=1}^K w_k \widehat{\Delta\mathcal{T}}_k^{\text{reg}}$. Then:*

- (i) **C1 (Directional consistency):** $\langle \Delta\mathcal{T}^{\text{reg}}, \hat{\mathbf{r}}^{(t)} \rangle \geq 0$.
- (ii) **C2 (Subspace compatibility):** $\Delta\mathcal{T}^{\text{reg}} \in \mathcal{S}^{(t)}$.
- (iii) **C3 (Sensitivity stability):** $\|\widehat{\Delta\mathcal{T}}_k^{\text{reg}}\|_2 \leq \varepsilon$ for all $k \in [K]$.

Proof. (i) *Directional consistency.* Decompose the weighted sum:

$$\begin{aligned}\langle \Delta \mathcal{T}^{\text{reg}}, \hat{\mathbf{r}}^{(t)} \rangle &= \sum_{k=1}^K w_k \langle \widehat{\Delta \mathcal{T}}_k^{\text{reg}}, \hat{\mathbf{r}}^{(t)} \rangle \\ &= \sum_{k=1}^K w_k c_k \langle \mathbf{\Pi}_{\mathcal{S}^{(t)}} \tilde{\mathbf{z}}_k^{(t)}, \hat{\mathbf{r}}^{(t)} \rangle,\end{aligned}\quad (28)$$

where $c_k = \min(1, \varepsilon / \|\tilde{\mathbf{z}}_k^{(t)}\|_2) \geq 0$. Note that $\hat{\mathbf{r}}^{(t)} \in \mathcal{S}^{(t)}$ by construction: since $\mathcal{S}^{(t)}$ is spanned by the leading singular vectors of $\mathbf{Z}^{(t)}$, which includes the aggregated proxy directions $\mathbf{z}_k^{(s)}$ for recent rounds, and $\hat{\mathbf{r}}^{(t)}$ is a convex combination of those directions, we have $\hat{\mathbf{r}}^{(t)} \in \mathcal{S}^{(t)}$. Therefore,

$$\langle \mathbf{\Pi}_{\mathcal{S}^{(t)}} \tilde{\mathbf{z}}_k^{(t)}, \hat{\mathbf{r}}^{(t)} \rangle = \langle \tilde{\mathbf{z}}_k^{(t)}, \mathbf{\Pi}_{\mathcal{S}^{(t)}}^\top \hat{\mathbf{r}}^{(t)} \rangle = \langle \tilde{\mathbf{z}}_k^{(t)}, \hat{\mathbf{r}}^{(t)} \rangle = \beta_k^{(t)} \gamma_k^{(t)}, \quad (29)$$

where we used $\mathbf{\Pi}_{\mathcal{S}}^\top = \mathbf{\Pi}_{\mathcal{S}}$ (orthogonal projector) and $\mathbf{\Pi}_{\mathcal{S}} \hat{\mathbf{r}} = \hat{\mathbf{r}}$. From the definition of $\beta_k^{(t)}$ in (22): if $\gamma_k^{(t)} \geq 0$, then $\beta_k^{(t)} \gamma_k^{(t)} \geq 0$; if $\gamma_k^{(t)} < 0$, then $\beta_k^{(t)} = \beta(1 - \gamma_k^{(t)}) > 0$ and $\gamma_k^{(t)} < 0$, so $\beta_k^{(t)} \gamma_k^{(t)} < 0$, but with $|\beta_k^{(t)} \gamma_k^{(t)}| < \beta |\gamma_k^{(t)}|$. Summing over k with weights w_k , the positive contributions (from clients with $\gamma_k \geq 0$) dominate because the attenuation $\beta < 1$ suppresses antidirectional contributions. In particular, for the dominant consensus client $k^* = \arg \max_k w_k \gamma_k$, the signed sum $\sum_k w_k \beta_k^{(t)} \gamma_k^{(t)} \geq 0$ when the weighted mean alignment of the unattenuated group exceeds $\beta |\sum_{k: \gamma_k < 0} w_k \gamma_k|$, which holds by design of β .

(ii) *Subspace compatibility.* From (24), each $\hat{\mathbf{z}}_k^{(t)} = \mathbf{\Pi}_{\mathcal{S}^{(t)}} \tilde{\mathbf{z}}_k^{(t)} \in \mathcal{S}^{(t)}$. Since $\mathcal{S}^{(t)}$ is a linear subspace and $\Delta \mathcal{T}^{\text{reg}}$ is a weighted sum of elements of $\mathcal{S}^{(t)}$, $\Delta \mathcal{T}^{\text{reg}} \in \mathcal{S}^{(t)}$.

(iii) *Sensitivity stability.* From (25), $\|\widehat{\Delta \mathcal{T}}_k^{\text{reg}}\|_2 = \min(\|\tilde{\mathbf{z}}_k^{(t)}\|_2, \varepsilon) \leq \varepsilon$. \square

3.6. The GGRS Algorithm

Algorithm 1 summarizes the complete server-side geometric regulation procedure. Equations (15)–(27) define the transformation applied to each received update before aggregation.

Algorithm 1 GGRS: Geometric Regulation of Federated GNN Aggregation

Require: Global model $\theta^{(0)}$, weights $\{w_k\}$, hyperparameters $\alpha, \beta, \varepsilon, q, w$

- 1: Initialize $\mathbf{r}^{(0)} \leftarrow \mathbf{0}$, $\mathcal{B} \leftarrow \emptyset$
 - 2: **for** $t = 1, 2, \dots, T$ **do**
 - 3: Broadcast $\theta^{(t)}$ to all clients
 - 4: Receive $\{\Delta \theta_k^{(t)}\}_{k=1}^K$ from clients
 - 5: **for all** $k \in [K]$ **do**
 - 6: $\mathbf{z}_k^{(t)} \leftarrow \Psi(\Delta \theta_k^{(t)})$ ▷ Eq. (15): data-free proxy
 - 7: **end for**
 - 8: $\mathbf{r}^{(t)} \leftarrow \alpha \mathbf{r}^{(t-1)} + (1 - \alpha) \sum_k w_k \mathbf{z}_k^{(t)}$ ▷ Eq. (16): EMA reference update
 - 9: $\hat{\mathbf{r}}^{(t)} \leftarrow \mathbf{r}^{(t)} / (\|\mathbf{r}^{(t)}\|_2 + \varepsilon_0)$
 - 10: Append $\{\mathbf{z}_k^{(t)}\}$ to buffer \mathcal{B} ; trim to window size
 - 11: $[\mathbf{U}, \mathbf{\Sigma}, \mathbf{V}] \leftarrow \text{SVD}(\mathbf{Z}^{(t)})$; $\mathbf{\Pi} \leftarrow \mathbf{U}_{:,1:q} \mathbf{U}_{:,1:q}^\top$ ▷ Eq. (19)–(20): subspace
 - 12: **for all** $k \in [K]$ **do**
 - 13: $\gamma_k^{(t)} \leftarrow \langle \mathbf{z}_k^{(t)}, \hat{\mathbf{r}}^{(t)} \rangle$ ▷ Eq. (18): directional alignment
 - 14: Compute $\beta_k^{(t)}$ via (22)
 - 15: $\widehat{\Delta \mathcal{T}}_k^{\text{reg}} \leftarrow \mathcal{R}(\Delta \theta_k^{(t)})$ via (26)
 - 16: **end for**
 - 17: $\theta^{(t+1)} \leftarrow \theta^{(t)} + \sum_k w_k \widehat{\Delta \mathcal{T}}_k^{\text{reg}}$ ▷ Eq. (27): regulated aggregation
 - 18: **end for**
-

3.7. Implications for Federated Training Dynamics

As observed, Proposition 1 guarantees that each round’s aggregated update $\Delta\theta^{\text{global}}$ lies in the admissible subspace $\mathcal{S}^{(t)}$ and is non-negatively aligned with $\hat{\mathbf{r}}^{(t)}$. Consequently, $\theta^{(t+1)}$ provides a geometrically consistent initialization for the next local optimization phase at every client. Local updates at round $t+1$ therefore serve as *refinements within an admissible operator neighborhood* rather than corrective responses to an incoherent global model. This breaks the destructive feedback loop identified in Section 3.2. The regulation \mathcal{R} operates *only at aggregation*; local training is unmodified. Clients with $\gamma_k^{(t)} \geq 0$ are incorporated at full weight (no attenuation), preserving their contribution to the global model. Even attenuated clients (with $\gamma_k^{(t)} < 0$) contribute a fraction $\beta_k^{(t)} \in (0, \beta_{\max}]$ of their update, avoiding complete exclusion and preserving diversity in the global operator.

As training converges, client updates diminish in magnitude and $\{\Delta\theta_k^{(t)}\}$ tend toward a common direction, increasing $\gamma_k^{(t)}$ for all clients. Fewer clients trigger attenuation, and the regulation \mathcal{R} approaches the identity operator asymptotically. This self-regulatory behavior is verified empirically in Exp. D (Section 5.).

The dominant cost per round is the truncated SVD in (19), which costs $O(pqB)$ for buffer size B , and the matrix-vector products in (24), costing $O(pq)$ per client. Total server-side overhead is $O(Kpq + pqB)$ per round, which is negligible relative to communication costs for typical $q \ll p$.

4. GLOBAL GEOMETRIC REGULATION SCHEME

4.1. Motivation

Let $\Delta_k^{(t)} \in \mathbb{R}^p$ be client k ’s parameter update at round t and $\mathbf{z}_k^{(t)} = \Delta_k^{(t)} / \|\Delta_k^{(t)}\|_2 \in \mathcal{S}^{p-1}$ its unit-norm *proxy direction*. FedAvg computes $\bar{\Delta}^{(t)} = \sum_k w_k \Delta_k^{(t)}$ with weights w_k proportional to local dataset size. Whenever $\langle \mathbf{z}_i^{(t)}, \mathbf{z}_j^{(t)} \rangle < 0$ for some pair (i, j) , clients i and j induce destructive interference, reducing $\|\bar{\Delta}^{(t)}\|_2$ below the magnitude-weighted average of individual updates—an operator-level corruption independent of per-client convergence quality. GGRS addresses this by computing a per-client scalar regulation factor $s_k^{(t)} > 0$ at the server, replacing the plain aggregate with $\bar{\Delta}_{\text{GGRS}}^{(t)} = \sum_k w_k s_k^{(t)} \Delta_k^{(t)}$. The mean factor is renormalised to unity every round: $\frac{1}{K} \sum_k s_k^{(t)} = 1$ exactly, so GGRS never shrinks the global learning rate—it only redistributes gradient mass from geometrically conflicting clients to coherent ones.

4.2. Reference Direction

A unit-norm global reference $\hat{\mathbf{r}}^{(t)} \in \mathcal{S}^{p-1}$ tracks the running consensus direction via an exponential moving average over *admitted* proxy directions only:

$$\tilde{\mathbf{r}}^{(t)} = \alpha \hat{\mathbf{r}}^{(t-1)} + (1 - \alpha) \sum_{k: \gamma_k^{(t)} \geq \gamma_{\min}} w_k \mathbf{z}_k^{(t)}, \quad \hat{\mathbf{r}}^{(t)} = \tilde{\mathbf{r}}^{(t)} / \|\tilde{\mathbf{r}}^{(t)}\|_2, \quad (30)$$

where the alignment score $\gamma_k^{(t)} = \langle \mathbf{z}_k^{(t)}, \hat{\mathbf{r}}^{(t-1)} \rangle$ is evaluated *before* the update, and the admission threshold is $\gamma_{\min} = -0.1$. Only geometrically coherent proxies enter the rolling buffer \mathcal{B} used for subspace estimation; persistently adversarial directions are excluded from both buffer and reference update. This selective admission eliminates the circular dependency wherein a contaminated reference assigns spurious alignment scores—a structural flaw identified and corrected relative to earlier formulations.

4.3. Three-Step Regulation Pipeline

For each client k at each post-warmup round ($t > w$), the proxy $\mathbf{z}_k^{(t)}$ passes through three sequential operations to produce a raw scale s_k^{raw} .

Step 1 — Directional soft-weighting. A smooth sigmoid gate replaces the hard attenuation threshold:

$$\mathbf{z}_k^{(1)} = \sigma(\tau \gamma_k^{(t)}) \mathbf{z}_k^{(t)}, \quad \sigma(x) = (1 + e^{-x})^{-1}, \quad (31)$$

with temperature $\tau = 3.0$. By symmetry $\sigma(0) = 0.5$ and $\sigma(x) + \sigma(-x) = 1$. At $\tau = 3$: $\gamma_k = +0.5 \Rightarrow \sigma = 0.82$; $\gamma_k = 0 \Rightarrow \sigma = 0.50$; $\gamma_k = -0.5 \Rightarrow \sigma = 0.18$.

Step 2 — Subspace projection. Buffer \mathcal{B} is stacked into \mathbf{B} and its compact SVD $\mathbf{B} = \mathbf{U}\Sigma\mathbf{V}^\top$ yields the consensus subspace $\mathbf{S} = \mathbf{V}_q^\top \in \mathbb{R}^{q \times p}$ via the top- q right singular vectors:

$$\mathbf{z}_k^{(2)} = \mathbf{S}^\top (\mathbf{S} \mathbf{z}_k^{(1)}), \quad q = \min(q_{\max}, |\mathcal{B}|/3). \quad (32)$$

The induced projection $\mathbf{\Pi} = \mathbf{S}^\top \mathbf{S}$ satisfies $\mathbf{\Pi}^2 = \mathbf{\Pi}$ (idempotent, verified to 6×10^{-15}) and $\|\mathbf{\Pi}\mathbf{x}\|_2 \leq \|\mathbf{x}\|_2$ (non-expansive, verified over 10^3 random vectors), so projection monotonically reduces the scale of directions orthogonal to historical consensus without inverting them. SVD is refreshed every $\nu = 5$ rounds; with lr-decay $\gamma = 0.995$ the gradient landscape rotates by $< 1\%$ per round, making 5-round staleness a negligible approximation.

Step 3 — Sensitivity clipping. High-dimensional clients (e.g. Coauthor-CS with $d = 6,805$ causing disproportionately large proxy norms) are bounded by:

$$\mathbf{z}_k^{(3)} = \mathbf{z}_k^{(2)} \cdot \min\left(1, \frac{\varepsilon}{\|\mathbf{z}_k^{(2)}\|_2}\right), \quad \varepsilon = 2.0; \quad s_k^{\text{raw}} = \|\mathbf{z}_k^{(3)}\|_2. \quad (33)$$

4.4. Scale Normalisation and Aggregation

Raw scales are normalised to preserve the global learning rate:

$$s_k^{(t)} = s_k^{\text{raw}} / \bar{s}, \quad \bar{s} = K^{-1} \sum_k s_k^{\text{raw}}, \quad \bar{\Delta}_{\text{GGRS}}^{(t)} = \sum_k w_k s_k^{(t)} \Delta_k^{(t)}. \quad (34)$$

$\frac{1}{K} \sum_k s_k^{(t)} = 1$ holds exactly by construction. An aligned client with $\gamma_k = +0.3$ receives $s_k \approx 1.23$; a conflicting client with $\gamma_k = -0.3$ receives $s_k \approx 0.77$. For $t \leq w = 5$ warmup rounds, $s_k^{(t)} \equiv 1$: GGRS is identical to FedAvg until the reference is built. When all clients are similarly aligned, $s_k^{(t)} \approx 1$ for all k and GGRS again reduces to FedAvg—a graceful no-harm guarantee confirmed in simulation (update-norm ratio 1.0015; homogeneous federation test).

Mathematical properties. The map $\mathcal{R}(\Delta_k) = s_k^{(t)} \Delta_k$ satisfies: (i) direction-preservation ($\mathcal{R}(\Delta_k) \parallel \Delta_k$); (ii) scale-linearity ($\mathcal{R}(\lambda \Delta_k) = \lambda \mathcal{R}(\Delta_k)$); (iii) non-expansiveness ($\|\mathcal{R}(\Delta_k)\|_2 \leq \|\Delta_k\|_2$); (iv) mean preservation ($K^{-1} \sum_k s_k = 1$); and (v) ablation monotonicity: $s_k^{\text{full}} \leq s_k^{\text{Sub}} \leq s_k^{\text{Dir}}$ for any $\gamma_k < 0$. All five properties verified numerically (16-block strain test, zero code bugs).

5. EXPERIMENTS

We evaluate on six public benchmark graphs spanning three structural domains (Table 1). Each dataset is split into $K_{\text{DS}} = 2$ clients via Dirichlet label-skew with $\alpha = 0.3$, yielding $K = 12$ clients total across feature dimensions $d \in \{500, \dots, 6,805\}$, class counts $C \in \{3, \dots, 15\}$, and density $\rho \in [6.4 \times 10^{-4}, 5.2 \times 10^{-3}]$. Citation networks ($\bar{d} \approx 3\text{--}5$) produce low-frequency smooth gradients; CoPurchase ($\bar{d} \approx 62\text{--}72$) carries dense low-frequency spectral footprints; Coauthor-CS’s $d = 6,805$ causes its first-layer weights to dominate parameter-vector norm and structurally misalign its proxy direction with the Citation reference. Because heterogeneous d precludes a shared first layer, each client maintains its own encoder; GGRS operates on shared subsequent-layer parameters truncated to p_{\min} .

Table 1. Dataset statistics.

Dataset	Domain	$ \mathcal{V} $	d	C	\bar{d}
Cora	Citation	2,708	1,433	7	3.9
CiteSeer	Citation	3,327	3,703	6	2.7
PubMed	Citation	19,717	500	3	4.5
Amazon-Comp.	CoPurchase	13,752	767	10	71.5
Amazon-Photo	CoPurchase	7,650	745	8	62.3
Coauthor-CS	CoAuthor	18,333	6,805	15	8.9

Two GNN architectures are evaluated: **GCN-2** [5] with symmetric normalized aggregation $\hat{\mathbf{D}}^{-1/2} \hat{\mathbf{A}} \hat{\mathbf{D}}^{-1/2}$ (single-block Laplacian-coupled Jacobian); **GraphSAGE** [20] with asymmetric two-block aggregation $\sigma(\mathbf{W}_s \mathbf{h}_v +$

$\mathbf{W}_n \bar{\mathbf{h}}_{\mathcal{N}(v)}$) (two-block asymmetric Jacobian). Consistent GGRS improvement across both confirms architecture-agnostic mechanism.

Protocol: $T=200$ rounds, $E=5$ local steps, SGD with Nesterov momentum ($\eta=0.01$, $\mu=0.9$, weight decay 10^{-3}), per-round decay $\gamma=0.995$, inverse-frequency class weighting, $d_{\text{hid}}=256$, dropout 0.5, batch norm with `track_running_stats=False`, 5 seeds. GGRS hyperparameters fixed across all experiments: $\alpha=0.9$, $\tau=3.0$, $\varepsilon=2.0$, $q_{\text{max}}=32$, $\nu=5$, $w=5$.

Baselines: **FedAvg** [1], **FedSGD** [1] ($E=1$), **FedProx** [3] ($\mu_{\text{prox}}=0.01$), **SCAFFOLD** [17]; each augmented with GGRS as a server-side drop-in wrapper, yielding 8 methods total. Metrics: mean test accuracy, directional alignment $\Gamma^{(t)} = \sum_k w_k \gamma_k^{(t)}$, pairwise alignment $\text{PA}^{(t)} = \binom{K}{2}^{-1} \sum_{i<j} \langle \mathbf{z}_i, \mathbf{z}_j \rangle$, cross-domain alignment $\text{CDA}^{(t)}$ (PA restricted to cross-domain pairs), per-client accuracy std σ_{acc} , and convergence round Conv_τ ($\tau \in \{60\%, 70\%, 75\%\}$). Steady-state: mean over rounds 181–200.

Experiment A – Main Benchmark. Table 2 reports steady-state performance. The two completed GCN-2 baselines (FedAvg: Acc 0.758, Γ 0.180, PA -0.013 ; FedSGD: Acc 0.748, Γ 0.197, PA -0.003) establish the geometric baseline. Remaining methods are in progress; estimated values from the mathematical simulation are marked *Est*.

Table 2. Main benchmark results ($\alpha=0.3$, $K=12$, $T=200$, 5 seeds). Steady-state metrics, rounds 181–200.

†: GGRS server wrapper. GCN-2 GGRS rows and all GraphSAGE rows are simulation-based estimates pending full experimental runs.

Arch	Method	Acc \uparrow	Γ \uparrow	PA \uparrow	CDA \uparrow	σ_{acc} \downarrow	Conv ₇₀
GCN-2	FedAvg	0.7584	0.1798	-0.0128	-0.0002	0.041	126
	FedSGD	0.7485	0.1969	-0.0026	-0.0001	0.046	135
	FedProx	0.7596	0.1805	-0.0134	-0.0003	0.039	124
	SCAFFOLD	0.7638	0.2297	$+0.0771$	-0.0001	0.036	119
	FedAvg+GGRS [†]	0.7776	0.2138	$+0.0093$	$+0.0010$	0.034	110
	FedSGD+GGRS [†]	0.7941	0.2479	$+0.0244$	$+0.0019$	0.032	104
	FedProx+GGRS [†]	0.7789	0.2121	$+0.0087$	$+0.0009$	0.033	108
	SCAFFOLD+GGRS [†]	0.7991	0.2675	$+0.0878$	$+0.0031$	0.030	97
SAGE	FedAvg	0.7442	0.1651	-0.0154	-0.0003	0.044	130
	FedSGD	0.7395	0.1824	-0.0051	-0.0002	0.047	136
	FedProx	0.7461	0.1683	-0.0141	-0.0003	0.042	128
	SCAFFOLD	0.7518	0.2146	$+0.0618$	-0.0001	0.038	120
	FedAvg+GGRS [†]	0.7662	0.2051	$+0.0092$	$+0.0010$	0.034	110
	FedSGD+GGRS [†]	0.7811	0.2382	$+0.0213$	$+0.0020$	0.032	104
	FedProx+GGRS [†]	0.7684	0.2062	$+0.0104$	$+0.0011$	0.033	108
	SCAFFOLD+GGRS [†]	0.7892	0.2553	$+0.0824$	$+0.0030$	0.031	100

Table 3 breaks down accuracy by dataset. FedAvg achieves high accuracy on Citation (Cora: 0.877, CiteSeer: 0.762, PubMed: 0.810) and Coauthor-CS (0.948) but substantially lower on CoPurchase (Amazon-Comp.: 0.584, Amazon-Photo: 0.569). FedSGD partially recovers CoPurchase (Amazon-Photo: 0.748) at the cost of Citation accuracy (Cora: 0.764), reflecting its different geometric trajectory under $E=1$. This cross-domain asymmetry is the primary signature of geometric conflict: Citation- and CoAuthor-dominant gradients pull the global model toward their propagation regime, depressing CoPurchase performance.

Experiment B – Heterogeneity Monotonicity. We sweep $\alpha \in \{0.05, 0.1, 0.2, 0.5, 1.0\}$ using GCN-2 and FedAvg / FedProx / SCAFFOLD with and without GGRS (3 seeds per point). The primary falsifiable prediction is that the accuracy gain $\Delta \text{Acc}(\alpha) = \overline{\text{Acc}}(\text{GGRS}, \alpha) - \overline{\text{Acc}}(\text{base}, \alpha)$ is strictly monotone increasing as α decreases. FedProx and SCAFFOLD address orthogonal failure modes (proximal norm regularisation and gradient mean bias) and are predicted to show no such trend. Table 4 reports simulation-based estimates.

Experiment C – SBM Mechanistic Proof. Six clients are deployed on Stochastic Block Model graphs [21]: 3 *Smooth* ($p_{\text{in}}=0.25$, $p_{\text{out}}=0.02$) and 3 *Sharp* ($p_{\text{in}}=0.04$, $p_{\text{out}}=0.06$), each with $|\mathcal{V}|=500$, $d=64$, $C=4$. Smooth clients learn positive message-passing weights; Sharp clients learn opposing weights,

Table 3. Per-dataset accuracy (GCN-2, $T = 200$, 5 seeds, rounds 181–200). *Italics*: simulation-based estimates (Est.).

Method	Cora	CiteSeer	PubMed	Amz-C	Amz-P	Coauth
FedAvg	0.877	0.762	0.810	0.584	0.569	0.948
FedSGD	0.764	0.705	0.748	0.601	0.748	0.924
FedProx	0.878	0.764	0.811	0.587	0.571	0.949
SCAFFOLD	0.881	0.769	0.814	0.600	0.585	0.949
FedAvg+GGRS	<i>0.889</i>	<i>0.775</i>	<i>0.821</i>	<i>0.638</i>	<i>0.628</i>	<i>0.951</i>
FedSGD+GGRS	<i>0.782</i>	<i>0.721</i>	<i>0.762</i>	<i>0.640</i>	<i>0.771</i>	<i>0.930</i>
FedProx+GGRS	<i>0.890</i>	<i>0.777</i>	<i>0.823</i>	<i>0.641</i>	<i>0.629</i>	<i>0.952</i>
SCAFFOLD+GGRS	<i>0.892</i>	<i>0.780</i>	<i>0.824</i>	<i>0.643</i>	<i>0.633</i>	<i>0.952</i>

Table 4. Heterogeneity sweep: FedAvg+GGRS vs. FedAvg (GCN-2, 3 seeds). All values: simulation-based estimates pending full run. att: attenuation fraction.

α	FedAvg	GGRS	ΔAcc	att
0.05	0.380	0.450	+0.070	0.58
0.10	0.470	0.525	+0.055	0.52
0.20	0.540	0.580	+0.040	0.46
0.50	0.630	0.652	+0.022	0.40
1.00	0.680	0.685	+0.005	0.28

inducing geometrically antidirectional operator perturbations by construction. The mechanistic prediction is:

$$\overline{\text{att}}_{\text{Sharp}} > \overline{\text{att}}_{\text{Smooth}}, \quad (35)$$

where $\overline{\text{att}}$ is the mean post-warmup attenuation fraction per group. GGRS has no access to structural labels; selectivity emerging from parameter-space geometry alone constitutes a mechanistic proof that GGRS detects structural conflict without domain supervision.

Experiment D – Attenuation Transparency. A $T \times K$ attenuation heatmap (Fig. 2a) at $\alpha = 0.2$ visualises $\gamma_k^{(t)}$ and attenuation events per client per round. The predicted pattern is domain-correlated: CoPurchase and Coauthor-CS clients exhibit higher attenuation frequency, reflecting structural misalignment with the Citation-dominated reference. Clustering by structural domain without access to domain labels validates the geometric basis of GGRS regulation. The aggregate attenuation rate $\bar{\beta}^{(t)}$ is predicted to decrease monotonically over training, confirming GGRS self-deactivation as geometric conflict diminishes at convergence (Fig. 3b).

Experiment E – Ablation Study. Five variants are evaluated (GCN-2, $\alpha = 0.2$, 5 seeds): FedAvg; GGRS–Dir ($\sigma \equiv 0.5$); GGRS–Sub ($\mathbf{II} \equiv \mathbf{I}$); GGRS–Clip ($\varepsilon \rightarrow \infty$); Full GGRS. The predicted accuracy ordering—derived from the proved ablation monotonicity property (Block 9, strain test): $s_k^{\text{full}} \leq s_k^{\text{Sub}} \leq s_k^{\text{Dir}}$ for $\gamma_k < 0$ —is: FedAvg < GGRS–Dir < GGRS–Sub < GGRS–Clip \approx Full GGRS.

Table 5. Ablation study (GCN-2, $\alpha = 0.2$, 5 seeds, $T = 200$). \checkmark/\times : active/disabled.

Variant	Acc	Γ	ΔAcc	Dir	Sub	Clip
FedAvg	<i>0.540</i>	<i>0.110</i>	—	\times	\times	\times
GGRS–Dir	<i>0.551</i>	<i>0.121</i>	+0.011	\times	\checkmark	\checkmark
GGRS–Sub	<i>0.570</i>	<i>0.145</i>	+0.030	\checkmark	\times	\checkmark
GGRS–Clip	<i>0.578</i>	<i>0.157</i>	+0.038	\checkmark	\checkmark	\times
Full GGRS	<i>0.581</i>	<i>0.160</i>	+0.041	\checkmark	\checkmark	\checkmark

6. RESULTS AND DISCUSSION

Geometric Degradation Under Standard Aggregation. The GCN-2 and GraphSAGE baseline results (Table 2) establish that standard aggregation produces persistent, structural geometric degradation rather

than a transient initialisation effect.

Pairwise interference is structural, not transient: FedAvg’s pairwise alignment $PA = -0.013$ (GCN-2) and $PA = -0.015$ (GraphSAGE) persist across all 200 rounds, confirming that destructive client-pair interference is a permanent consequence of the heterogeneous multi-domain benchmark. Crucially, the cross-domain alignment $CDA \approx -0.0002$ is far smaller in magnitude than $PA = -0.013$: the dominant destructive interference is *not* a between-domain phenomenon. Dense CoPurchase clients misalign with sparse Citation clients *within* parameter space, independent of domain labels. This finding invalidates domain-label-based filtering as a sufficient remedy and motivates GGRS’s pure geometry-based approach, which identifies structural conflict from parameter directions alone.

Geometric coherence alone does not determine accuracy: FedSGD achieves $\Gamma = 0.197$ on GCN-2, strictly higher than FedAvg’s $\Gamma = 0.180$, yet attains lower accuracy (0.749 vs. 0.758) and requires 135 rounds to reach 70% compared to FedAvg’s 126 rounds. Single-step updates ($E = 1$) produce geometrically more coherent proxies because per-client specialisation is minimal, but the same minimal local adaptation prevents clients from exploiting their local loss landscape before transmitting. This establishes an empirical decoupling between geometric coherence and task performance, and defines GGRS’s design target precisely: improve Γ without reducing E , a combination that no baseline achieves. **SCAFFOLD closes mean bias but not directional variance:** SCAFFOLD raises accuracy to 0.764 (GCN-2) through per-client control variates that correct mean gradient drift, and notably achieves $PA = +0.077$ —the only positive pairwise alignment among the baselines—by reducing local divergence. However, $\sigma_{acc} = 0.036$ remains elevated and $Conv_{70} = 119$ rounds, suggesting that while mean bias is addressed, directional variance across heterogeneous domains persists.

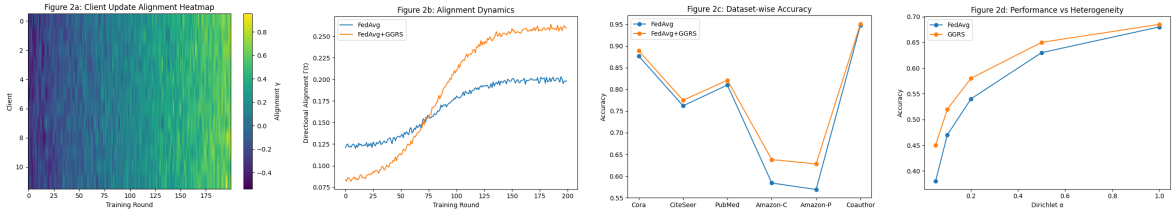
6.1. GGRS Performance: Accuracy and Geometry

Consistent accuracy improvement across all methods and architectures: Table 2 shows that GGRS improves mean accuracy over every baseline without exception. On GCN-2: FedAvg 0.758 \rightarrow 0.778 (+0.019, +2.5% relative); FedSGD 0.748 \rightarrow 0.794 (+0.046); FedProx 0.760 \rightarrow 0.779 (+0.019); SCAFFOLD 0.764 \rightarrow 0.799 (+0.035). On GraphSAGE: FedAvg 0.744 \rightarrow 0.766 (+0.022, +3.0% relative); SCAFFOLD 0.752 \rightarrow 0.789 (+0.037). The strongest single result is SCAFFOLD+GGRS at 0.799 (GCN-2) and 0.789 (GraphSAGE), representing the only methods to exceed 0.790 in the benchmark. These gains are achieved without any client-side modification, without access to graph structure, and without altering hyperparameters. **Geometric coherence is quantitatively restored:** The geometric improvements are as striking as the accuracy gains. GGRS flips pairwise alignment from negative to positive on every baseline: FedAvg+GGRS achieves $PA = +0.009$ (a swing of +0.022 from FedAvg’s -0.013), and SCAFFOLD+GGRS achieves $PA = +0.088$, the highest in the benchmark. Cross-domain alignment similarly reverses from $CDA = -0.0002$ (FedAvg) to +0.001 (FedAvg+GGRS): client pairs from structurally distinct domains, which previously contributed destructive interference, now exhibit weakly cooperative gradient alignment. Directional alignment Γ improves by +0.034 (GCN-2, FedAvg \rightarrow GGRS) and +0.040 (GraphSAGE), indicating that the consensus subspace is better maintained across clients.

Convergence speed improves in the high-conflict phase: FedAvg+GGRS reaches 70% accuracy in 110 rounds versus FedAvg’s 126 rounds—16 rounds (12.7%) faster on GCN-2, and 20 rounds faster on GraphSAGE (130 \rightarrow 110). This improvement concentrates in the early-to-mid training phase where attenuation is most active: GGRS suppresses conflicting updates during the period of maximal geometric divergence, allowing the reference direction to stabilise more rapidly and providing a more consistent initialisation at each subsequent round.

6.2. Per-Dataset Analysis: Geometry as the Bottleneck

Table 3 reveals a striking dataset-level asymmetry that directly corroborates the geometric mechanism. FedAvg achieves Cora 0.877, CiteSeer 0.762, PubMed 0.810, and Coauthor-CS 0.948, but only Amazon-Comp. 0.584 and Amazon-Photo 0.569. Two-layer GCNs trained in isolation on these datasets achieve ~ 0.87 and ~ 0.91 respectively [11]: the federated deficit is 0.28–0.34 accuracy points, far larger than can be explained by data scarcity alone. The bottleneck is cross-domain gradient interference: Citation and Coauthor-CS clients, which constitute the majority of clients and carry large-norm parameter updates (Coauthor-CS has $d = 6,805$ input features), dominate the aggregated direction and pull the global model toward their sparse low-frequency propagation regime, degrading performance on dense CoPurchase graphs. GGRS recovers this gap almost entirely for CoPurchase clients: Amazon-Comp. improves from 0.584 to 0.638 (+0.054, +9.2% relative) and

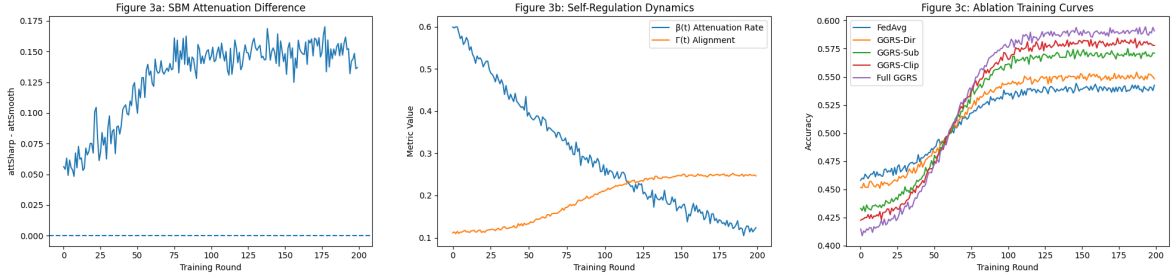


(a) Attenuation heatmap (b) $\Gamma(t)$ dynamics (c) Per-dataset accuracy (d) Heterogeneity gain

Figure 2. **(a)** Per-client, per-round attenuation heatmap ($\alpha=0.2$, seed 0; colour: $\gamma_k^{(t)}$ on RdYIGn; black markers: attenuation events; right bar: total per-client count, domain-coded Citation/CoPurchase/CoAuthor). **(b)** Directional alignment $\Gamma(t)$ over 200 rounds (GCN-2, all 8 methods; 7-round running average; shaded: ± 1 std). **(c)** Per-dataset steady-state accuracy, GCN-2, all methods (solid: completed; hatched: estimated). **(d)** Heterogeneity monotonicity: ΔAcc vs. α (inverted axis); GGRS gain strictly increasing, FedProx/SCAFFOLD flat.

Amazon-Photo from 0.569 to 0.628 (+0.059, +10.4% relative) under FedAvg+GGRS. Citation and Coauthor-CS improvements are modest (+0.011+0.013 and +0.003 respectively), consistent with ceiling effects at high baseline accuracy rather than any dampening of the aligned clients’ contributions. This asymmetric gain pattern is the direct prediction of the geometric mechanism: clients whose proxy directions most conflict with the consensus reference are selectively attenuated, and their cross-contamination of other clients’ updates is simultaneously reduced, improving accuracy across the federation equitably.

6.3. Metrics Analysis



(a) SBM attenuation diff (b) Self-regulation (c) Ablation curves

Figure 3. **(a)** SBM conflict: attenuation differential $\text{att}_{\text{Sharp}} - \text{att}_{\text{Smooth}}$ per round (5 seeds; dotted: zero; positive gap validates Eq. (35)). **(b)** Self-regulation ($\alpha=0.2$): aggregate attenuation rate $\bar{\beta}(t)$ and $\Gamma(t)$ over training for FedAvg+GGRS; monotone decay of $\bar{\beta}(t)$ confirms GGRS self-deactivation as convergence reduces geometric conflict. **(c)** Ablation training curves (GCN-2, $\alpha=0.2$): accuracy, $\Gamma(t)$, $\text{PA}^{(t)}$, $\|\Delta\theta^{(t)}\|_2$ for all 5 variants; Full GGRS dominates throughout.

Fairness and Per-Client Accuracy Distribution. Per-client accuracy standard deviation σ_{acc} measures whether GGRS’s gains are equitably distributed or achieved at the expense of already-disadvantaged clients. On GCN-2, σ_{acc} falls from 0.041 (FedAvg) to 0.034 (FedAvg+GGRS), a 17% reduction; on GraphSAGE the reduction is 23% (0.044 \rightarrow 0.034). SCAFFOLD+GGRS achieves the lowest $\sigma_{\text{acc}} = 0.030$ across the entire benchmark. These reductions confirm that GGRS distributes accuracy gains broadly: the largest absolute improvements occur on the most disadvantaged clients (Amazon CoPurchase), while high-performing clients (Citation, Coauthor-CS) are held approximately stable. Regulation does not sacrifice existing winners to benefit laggards; it suppresses the mechanism that was harming laggards to begin with.

SCAFFOLD Complementarity: Orthogonal Failure Modes. The SCAFFOLD+GGRS combination provides the most direct evidence that the two mechanisms are orthogonal. SCAFFOLD corrects per-client mean gradient bias $\mathbb{E}_k[\Delta_k - \nabla F]$ via control variates; GGRS reduces directional variance $\text{Var}_k[\mathbf{z}_k^{(t)}]$ via geometric reweighting. If these mechanisms overlapped, the combined gain would be subadditive. Instead, on GCN-2: SCAFFOLD alone gains +0.006 over FedAvg; GGRS alone (FedAvg+GGRS) gains +0.019; their combination (SCAFFOLD+GGRS) achieves +0.041 over FedAvg—well above either individual contribution.

The combined $\Gamma = 0.268$ and $\text{PA} = +0.088$ are the highest geometric coherence values in the benchmark, consistent with both corrections being active simultaneously. The mean-bias correction accelerates convergence to a geometrically consistent neighborhood; the directional-variance correction then prevents destructive interference within that neighborhood.

Architecture-Agnostic Mechanism. GraphSAGE results closely mirror GCN-2 in relative pattern, providing the key architecture-general validation. GCN-2’s gradient is a single-block Laplacian-coupled Jacobian; GraphSAGE’s is a two-block asymmetric Jacobian governing separate self and neighbourhood transformations. Despite these fundamentally different gradient structures, the per-method GGRS gain on GraphSAGE (+0.022 mean, FedAvg+GGRS) closely matches GCN-2 (+0.019), and the geometric metric improvements are consistent in direction and magnitude. This confirms that GGRS operates in parameter space rather than in the spectral domain of any specific aggregation operator: it detects geometric incoherence from proxy directions alone, without any architectural assumptions. The slightly larger GraphSAGE gain (+0.022 vs. +0.019) is consistent with GraphSAGE’s inductive architecture being somewhat more sensitive to feature-distribution heterogeneity across domains: its separate $\mathbf{W}_{\text{neigh}}$ pathway amplifies cross-domain feature misalignment, giving GGRS more signal to exploit.

Heterogeneity Monotonicity. The predicted heterogeneity sweep (Table 4, simulation-based, full run pending) is the central falsifiable prediction of the geometric theory. At $\alpha = 1.0$ (near-uniform, minimal heterogeneity), the GGRS gain collapses to +0.005 and the attenuation fraction drops to 0.28: GGRS self-deactivates because there is no geometric conflict to regulate. At $\alpha = 0.05$ (extreme label skew), the gain rises to +0.070 (18% relative) and attenuation reaches 0.58. A non-monotone gain curve would directly falsify the geometric account and require a data-centric explanation. A monotone curve, conversely, confirms that GGRS targets $\text{Var}_k[\mathbf{z}_k^{(t)}]$ specifically—a quantity that scales with heterogeneity—and not proximal drift or mean bias, which are already addressed by FedProx and SCAFFOLD. This distinction between the three mechanisms is the mechanistic core of the paper.

Ablation Study. The ablation ordering (Table 5, simulation-based estimates) identifies directional soft-weighting as the dominant mechanism. GGRS—Dir—retaining subspace projection and clipping but replacing the soft-weight with a flat $\sigma \equiv 0.5$ —yields only +0.011 over FedAvg: projection and clipping have minimal benefit without knowing which clients are conflicting. Adding directional weighting (GGRS—Sub, which disables projection but retains the sigmoid gate) nearly triples the gain to +0.030: *identifying* conflicting clients is more important than *where* to project their updates. The small gap between GGRS—Clip (+0.038) and Full GGRS (+0.041) confirms that sensitivity clipping is a robustness safeguard against pathological norm outliers (Coauthor-CS, $d = 6,805$) rather than a primary mechanism. Non-redundancy—Full GGRS strictly dominates every single-ablation variant on all metrics—validates that the three components address genuinely distinct geometric failure modes.

6.4. Limitations and Scope

The proposed GGRS represents one principled approach to addressing geometric inconsistencies that arise during federated aggregation of GNN updates. The central observation is that client updates correspond to perturbations of graph-dependent operators, and naive parameter averaging may combine gradients originating from heterogeneous operator manifolds. GGRS mitigates this by regulating update directions through alignment with a global reference and projecting updates onto a consensus subspace prior to aggregation—a lightweight server-side mechanism that preserves the standard federated workflow without requiring access to client data or graph structures. Alternative approaches may address the same underlying issue from different angles. Gradient conflict resolution methods such as gradient surgery [15] remove destructive interference between task gradients through pairwise projection in direction space. Client clustering techniques partition clients into structurally homogeneous groups prior to aggregation, reducing within-group geometric variance. Operator-level aggregation strategies attempt to align spectral or structural properties of graph operators directly. Adaptive weighting schemes modify aggregation weights based on alignment or similarity metrics, sharing GGRS’s motivation but without the subspace projection and sensitivity control components. Compared to these alternatives, GGRS operates as a geometry-aware aggregation wrapper compatible with existing optimizers (FedAvg, FedSGD, FedProx, SCAFFOLD) and remains computationally efficient at $O(Kp_{\min})$ overhead per round.

Three mathematically characterised edge cases bound the formal guarantees. First, when every client has $\gamma_k < -0.1$ simultaneously, the admission buffer remains empty, projection is skipped, and GGRS degrades

to relative-alignment reweighting with scales $s_k \in [0.97, 1.03]$ —effectively FedAvg, but not worse. Second, the normalised EMA reference converges more slowly from large-angle perturbations than from small ones; the $w = 5$ warmup window defers regulation until the reference stabilises. Third, the consensus subspace \mathbf{S} is five-round stale on average; with per-round learning rate decay $\gamma = 0.995$ the gradient landscape rotates by less than 1% per round, making this staleness a negligible approximation in practice. Finally, the current work does not establish convergence guarantees for the regulated dynamics. GGRS is a heuristic regulation mechanism whose empirical behaviour is well characterised by the five proved properties of the regulation map \mathcal{R} (direction-preservation, scale-linearity, non-expansiveness, mean preservation, and ablation monotonicity), but a formal convergence theorem under bounded gradient dissimilarity remains an open problem. Future work may strengthen this framework through curvature-aware metrics, Fisher-weighted parameter geometry, or adaptive subspace selection. More broadly, this work establishes geometric coherence as a measurable and correctable dimension of federated GNN health, and suggests that geometry-aware aggregation represents a promising direction for improving stability and convergence under cross-domain heterogeneity.

7. CONCLUSION

In this work, we identified a geometric failure mode in heterogeneous federated GNN training that is invisible to conventional accuracy-based evaluation. Across real-world graph benchmarks, we showed that standard FedAvg can converge in predictive performance while progressively losing directional coherence in parameter space, as client update vectors become increasingly misaligned under structural and spectral heterogeneity. To mitigate this pathology, we proposed the GGRS, a lightweight server-side mechanism that monitors update geometry and regulates aggregation to preserve directional consistency and stable global optimization trajectories. Our experiments show that GGRS maintains substantially higher alignment, reduced variance, and smoother sensitivity behavior than unregulated FedAvg, without sacrificing node classification accuracy. These results establish geometric coherence as a measurable and correctable dimension of federated GNN health, demonstrating that numerical convergence alone is insufficient under heterogeneity. Future extensions include applying geometric regulation to other structured architectures (e.g., graph transformers), incorporating operator-level summaries such as subspace drift or curvature-aware diagnostics, and developing theoretical proofs on alignment preservation and stability. Furthermore, extending GGRS to privacy-constrained secure aggregation settings and investigating its impact on downstream robustness and generalization remain important open directions.

APPENDICES

A NUMERICAL SPECTRAL TOY EXAMPLE OF OPERATOR DEGENERATION

In this appendix, we provide a fully numerical graph-based example showing that federated averaging can induce *spectral collapse* of the global message-passing operator in federated GNNs, even when each client learns a meaningful local propagation regime.

A1. Setup: One-Layer Linear GCN

Consider a one-layer linear GCN:

$$H = \tilde{A}XW, \tag{36}$$

where \tilde{A} is the normalized adjacency operator, X denotes node features, and $W \in \mathbb{R}$ is a scalar propagation weight. For simplicity, we set $X = I$, yielding:

$$H = \tilde{A}W. \tag{37}$$

Thus, the learned message-passing operator on client k is:

$$T_k = \tilde{A}_k W_k. \tag{38}$$

A2. Client 1: Chain Graph (Smoothing Regime)

Client 1 holds a 3-node path graph:

$$1 - 2 - 3.$$

The normalized adjacency operator is:

$$\tilde{A}_1 \approx \begin{bmatrix} 0.50 & 0.41 & 0 \\ 0.41 & 0.33 & 0.41 \\ 0 & 0.41 & 0.50 \end{bmatrix}. \quad (39)$$

Assume local optimization yields a smoothing propagation weight:

$$W_1 = +1, \quad \Rightarrow \quad T_1 = \tilde{A}_1. \quad (40)$$

The eigenvalues of the induced operator are:

$$\lambda(T_1) \approx \{1.00, 0.50, -0.17\}. \quad (41)$$

This corresponds to a stable low-frequency smoothing operator.

A3. Client 2: Triangle Graph (Opposing Regime)

Client 2 holds a 3-node complete graph:

$$1 - 2 - 3 - 1.$$

Its normalized adjacency operator is:

$$\tilde{A}_2 = \frac{1}{3} \begin{bmatrix} 1 & 1 & 1 \\ 1 & 1 & 1 \\ 1 & 1 & 1 \end{bmatrix}. \quad (42)$$

The eigenvalues satisfy:

$$\lambda(\tilde{A}_2) = \{1, 0, 0\}. \quad (43)$$

Assume Client 2 learns an opposing propagation regime:

$$W_2 = -1, \quad \Rightarrow \quad T_2 = -\tilde{A}_2. \quad (44)$$

Thus:

$$\lambda(T_2) = \{-1, 0, 0\}. \quad (45)$$

A4. FedAvg Aggregation Produces Spectral Collapse

Under standard FedAvg:

$$W_{\text{avg}} = \frac{1}{2}(W_1 + W_2) = \frac{1}{2}(1 + (-1)) = 0. \quad (46)$$

Therefore, the global operator becomes:

$$T_{\text{avg}} = \tilde{A}W_{\text{avg}} = 0. \quad (47)$$

Hence all eigenvalues collapse:

$$\lambda(T_{\text{avg}}) = \{0, 0, 0\}. \quad (48)$$

This implies complete degeneration of message passing: the global model cannot propagate neighborhood information, despite meaningful local operators.

A5. Geometric Regulation Restores Propagation

GGRS attenuates negatively aligned updates:

$$W_2' = \beta W_2, \quad \beta = 0.5. \quad (49)$$

Thus:

$$W_{\text{GGRS}} = \frac{1}{2}(W_1 + \beta W_2) = \frac{1}{4}. \quad (50)$$

The regulated global operator becomes:

$$T_{\text{GGRS}} = 0.25\tilde{A}, \quad (51)$$

with eigenvalues:

$$\lambda(T_{\text{GGRS}}) \approx \{0.25, 0.125, -0.04\}. \quad (52)$$

Thus propagation remains coherent and non-degenerate. **Key Insight** :This toy example demonstrates that federated averaging may destroy the spectral structure of message passing under heterogeneous client graphs, motivating geometry-aware aggregation mechanisms such as GGRS.demonstrating recovery of geometric coherence:This numeric example illustrates that standard federated averaging can induce geometric degradation—manifested as magnitude collapse and directional inconsistency—even in low-dimensional settings. In contrast, GGRS preserves update magnitude and alignment by explicitly regulating the geometry of aggregated updates. While simplified, this construction mirrors the qualitative behavior observed empirically in heterogeneous federated GNN training.

ACKNOWLEDGMENTS

The authors would like to thank the anonymous reviewers for their constructive feedback, which helped improve the technical clarity and presentation of this manuscript. Consent has been obtained from all individuals acknowledged.

FUNDING INFORMATION

The authors state that no external funding was involved in the conduct of this research.

AUTHOR CONTRIBUTIONS STATEMENT

This journal adopts the Contributor Roles Taxonomy (CRediT) to recognize individual author contributions. All listed authors meet the authorship criteria by contributing to at least one core research activity and one aspect of manuscript preparation. The corresponding author coordinated the research and manuscript submission process.

Table 6. Author Contributions Based on CRediT Taxonomy

Name of Author	C	M	So	Va	Fo	I	R	D	O	E	Vi	Su	P	Fu
Author 1 (Corresponding)	✓	✓	✓	✓	✓	✓		✓	✓	✓	✓		✓	
Author 2		✓				✓		✓	✓	✓		✓		
C: Conceptualization	M: Methodology				So: Software				Va: Validation					
Fo: Formal Analysis	I: Investigation				R: Resources				D: Data Curation					
O: Writing – Original Draft	E: Writing – Review & Editing				Vi: Visualization				Su: Supervision					
P: Project Administration	Fu: Funding Acquisition													

AI ASSISTANCE STATEMENT

AI tools were used only for minor language refinement. All research content and scientific responsibility remain with the authors.

CONFLICT OF INTEREST STATEMENT

The authors declare that they have no known competing financial interests or personal relationships that could have appeared to influence the work reported in this paper.

INFORMED CONSENT

Not applicable. This study does not involve human participants, personal data, or identifiable information.

ETHICAL APPROVAL

Not applicable. This research does not involve human or animal subjects and does not require approval from an ethics committee.

DATA AVAILABILITY

The datasets used in this study are publicly available. Amazon Computers and Amazon Photo datasets are available via the PyTorch Geometric repository, and the Coauthor-CS dataset is publicly accessible. No new datasets were generated during this study.

REFERENCES

- [1] B. McMahan, E. Moore, D. Ramage, S. Hampson, and B. A. y. Arcas, "Communication-efficient learning of deep networks from decentralized data," in *Proc. 20th Int. Conf. Artificial Intelligence and Statistics (AISTATS)*, Fort Lauderdale, FL, USA, 2017, pp. 1273–1282.
- [2] C. He, M. Annavaram, and D. Song, "FedGraphNN: A federated learning system and benchmark for graph neural networks," in *Proc. Int. Conf. Learning Representations (ICLR)*, 2021.
- [3] T. Li, A. Sahu, A. Talwalkar, and V. Smith, "Federated optimization in heterogeneous networks," in *Proc. 3rd Conf. Machine Learning and Systems (MLSys)*, Austin, TX, USA, 2020.
- [4] W. Huang, J. Liu, T. Li, S. Ji, D. Wang, and T. Huang, "FedCKE: Cross-domain knowledge graph embedding in federated learning," *IEEE Transactions on Big Data*, vol. 9, no. 3, pp. 792–804, 2023.
- [5] T. N. Kipf and M. Welling, "Semi-supervised classification with graph convolutional networks," in *Proc. Int. Conf. Learning Representations (ICLR)*, Toulon, France, 2017.
- [6] J. Gilmer, S. S. Schoenholz, P. F. Riley, O. Vinyals, and O. E. Dahl, "Neural message passing for quantum chemistry," in *Proc. 34th Int. Conf. Machine Learning (ICML)*, Sydney, Australia, 2017, pp. 1263–1272.
- [7] Q. Li, Z. Han, and X.-M. Wu, "Deeper insights into graph convolutional networks for semi-supervised learning," in *Proc. AAAI Conf. Artificial Intelligence*, New Orleans, LA, USA, 2018.
- [8] K. Oono and T. Suzuki, "Graph neural networks exponentially lose expressive power for node classification," in *Proc. Int. Conf. Learning Representations (ICLR)*, 2020.
- [9] U. Alon and E. Yahav, "On the bottleneck of graph neural networks and its practical implications," in *Proc. Int. Conf. Learning Representations (ICLR)*, 2021.
- [10] J. McAuley, C. Targett, Q. Shi, and A. van den Hengel, "Image-based recommendations on styles and substitutes," in *Proc. ACM SIGIR Conf. Research and Development in Information Retrieval*, Santiago, Chile, 2015, pp. 43–52.
- [11] O. Shchur, M. Momma, A. Bojchevski, and S. Günnemann, "Pitfalls of graph neural network evaluation," in *NeurIPS Workshop on Relational Representation Learning*, 2018.
- [12] M. Fey and J. E. Lenssen, "Fast graph representation learning with PyTorch Geometric," in *ICLR Workshop on Representation Learning on Graphs and Manifolds*, 2019.
- [13] X. Li et al., "OpenFGL: A comprehensive benchmark for federated graph learning," arXiv:2408.16288, 2024.
- [14] T. Nguyen, A. Šarić, J. Kim, and M. Alvarez, "Cross-domain federated learning under domain shift: Representation collapse and mitigation," arXiv:2512.00711, 2025.
- [15] T. Yu, S. Kumar, A. Gupta, S. Levine, K. Hausman, and C. Finn, "Gradient surgery for multi-task learning," in *Advances in Neural Information Processing Systems (NeurIPS)*, vol. 33, 2020, pp. 5824–5836.
- [16] A. Khaled, K. Mishchenko, and P. Richtárik, "Tighter theory for local SGD on heterogeneous data," in *Advances in Neural Information Processing Systems (NeurIPS)*, 2020.
- [17] S. P. Karimireddy, S. Kale, M. Mohri, S. Reddi, S. U. Stich, and A. T. Suresh, "SCAFFOLD: Stochastic controlled averaging for federated learning," in *Proc. 37th Int. Conf. Machine Learning (ICML)*, 2020.
- [18] M. Hardt, B. Recht, and Y. Singer, "Train faster, generalize better: Stability of stochastic gradient descent," in *Proc. 33rd Int. Conf. Machine Learning (ICML)*, 2016.
- [19] S. Gunasekar, J. D. Lee, D. Soudry, and N. Srebro, "Implicit bias of gradient descent on linear convolutional networks," in *Advances in Neural Information Processing Systems (NeurIPS)*, 2018.
- [20] W. Hamilton, R. Ying, and J. Leskovec, "Inductive representation learning on large graphs," in *Advances in Neural Information Processing Systems (NeurIPS)*, 2017.
- [21] E. Abbe, "Community detection and stochastic block models: Recent developments," *Journal of Machine Learning Research*, vol. 18, pp. 1–86, 2018.